Journal of Non-Newtonian Fluid Mechanics 237 (2016) 54–64

Contents lists available at ScienceDirect

Journal of Non-Newtonian Fluid Mechanics

journal homepage: www.elsevier.com/locate/jnnfm

Second-gradient modelling of orientation development and rheology of dilute confined suspensions

A. Scheuer[a,b], E. Abisset-Chavanne[a], F. Chinesta[a,*], R. Keunings[b]

[a] ESI Group Chair & ICI - High Performance Computing Institute, Ecole Centrale de Nantes, 1 Rue de la Noe, Nantes F-44300, France
[b] ICTEAM, Université catholique de Louvain, Bat. Euler, Av. Georges Lemaitre 4, Louvain-la-Neuve, B-1348, Belgium

ARTICLE INFO

Article history:
Received 28 May 2016
Revised 18 October 2016
Accepted 20 October 2016
Available online 22 October 2016

Keywords:
Confinement
Fibre suspensions
Jeffery's equation
Poiseuille and squeeze flows

ABSTRACT

We address the extension of Jeffery's model, governing the orientation of rods immersed in a Newtonian fluid, to confined regimes occurring when the thickness of the flow domain is narrower than the rod length. The main modelling ingredients concern: (i) the consideration of the rod interactions with one or both gap walls and their effects on the rod orientation kinematics; and (ii) the consideration of non-uniform strain rates at the scale of the rod, requiring higher-order descriptions. Such scenarios are very close to those encountered in real composites forming processes and have never been appropriately addressed from a microstructural point of view. We also show that confinement conditions affect the rheology of the suspension.

1. Introduction

Short fibre-reinforced polymer composites are widely used in manufacturing industries to produce lightweight structural and functional parts with enhanced mechanical properties. Forming processes commonly involve injection or compression moulding, where the short fibre composite behaves as a fibre suspension. The orientation of the fibres is impacted by the flowing matrix and interactions with the neighbouring fibres and cavity walls. Predicting the evolution of the orientation state can be extremely complex, and changes in fibre orientation correspond to changes in the final mechanical properties of the part. Thus, modelling tools are of crucial importance to predict the orientation of fibres during the process and were the subject of intense research over the last decades.

Fibre suspensions can be described at three different scales: (i) the *microscopic* scale, the scale of the fibre; (ii) the *mesoscopic* scale, the scale of a population of fibres; and (iii) the *macroscopic* scale, the scale of the part.

Most models used to describe such suspensions are built upon Jeffery's pioneering work. In his classical 1922 paper [11], Jeffery studied the evolution of the orientation of a rigid ellipsoid suspended in a Newtonian fluid in a Stokes flow field and showed that particles rotate about the vorticity axis. The orientation of the particle is then given by the time evolution of a unit vector $\mathbf{p}$ aligned with the fibre axis. Particularized to rods (infinite aspect-ratio ellipsoids), the microscopic Jeffery equation thus reads

$$\dot{\mathbf{p}} = \boldsymbol{\Omega}\cdot\mathbf{p} + (\mathbf{D}\cdot\mathbf{p} - (\nabla\mathbf{v} : (\mathbf{p}\otimes\mathbf{p}))\mathbf{p}), \tag{1}$$

where $\mathbf{D} = \frac{1}{2}(\nabla\mathbf{v} + (\nabla\mathbf{v})^T)$ and $\boldsymbol{\Omega} = \frac{1}{2}(\nabla\mathbf{v} - (\nabla\mathbf{v})^T)$ are respectively the symmetric and skew-symmetric components of the velocity gradient $\nabla\mathbf{v}$.

At the mesoscopic scale, the individuality of fibres is lost in favour of a statistical description of a population of fibres, and the conformation is given by $\psi(\mathbf{x}, t, \mathbf{p})$, the probability density function – pdf – giving for each position $\mathbf{x}$ and time t, the fraction of fibres aligned along direction $\mathbf{p}$. The evolution of the pdf follows a Fokker–Planck equation:

$$\frac{\partial\psi}{\partial t} + \nabla_x\cdot(\dot{\mathbf{x}}\,\psi) + \nabla_p\cdot(\dot{\mathbf{p}}\,\psi) = 0, \tag{2}$$

where $\dot{\mathbf{x}} = \mathbf{v}(\mathbf{x}, t)$ and the rod rotary velocity $\dot{\mathbf{p}}$ is given by Jeffery's equation.

Finally, at the macroscopic scale, we coarsen a little bit more to derive macroscopic descriptors defined in standard physical domains (i.e. only space and time). The pdf is thus substituted by some of its moments [3]. The first two non-zero moments are then the second-order moment or second-order orientation tensor

$$\mathbf{a} = \int_{\mathcal{S}} (\mathbf{p}\otimes\mathbf{p})\;\psi(\mathbf{p})\;\mathrm{d}\mathbf{p} \tag{3}$$

and the fourth-order moment

$$\mathbf{A} = \int_{\mathcal{S}} (\mathbf{p}\otimes\mathbf{p}\otimes\mathbf{p}\otimes\mathbf{p})\;\psi(\mathbf{p})\;\mathrm{d}\mathbf{p}. \tag{4}$$

* Corresponding author.
E-mail addresses: Adrien.Scheuer@ec-nantes.fr, Adrien.Scheuer@uclouvain.be (A. Scheuer), Emmanuelle.Abisset-Chavanne@ec-nantes.fr (E. Abisset-Chavanne), Francisco.Chinesta@ec-nantes.fr (F. Chinesta), Roland.Keunings@uclouvain.be (R. Keunings).

http://dx.doi.org/10.1016/j.jnnfm.2016.10.004
0377-0257/

A wide literature [4,8–10], developed upon Jeffery's theory, is available and richer models were proposed. We refer to the review by Petrie [14] and the reference therein for an overview of the rheology of fibre suspensions. In particular, the well-known Folgar–Tucker model [7] accurately models the effect of fibre-fibre interactions in the semi-dilute and semi-concentrated regimes by adding a randomizing diffusion term to Jeffery's model.

Model predictions using the Folgar–Tucker model compared to experimental results suggest however that the rate of fibre orientation is slower than theory predicts. Hence, the models were further enriched [6,15,17,18] in order to take into account the observed delay (attributed for a long time to fibre-fibre interactions), either by introducing a "slip" parameter in the model or by taking into account interaction mechanisms in a multi-scale approach. In [13], we pointed out the impact that confinement can have on the orientation kinematics of suspended fibres in flow processes with narrow gaps, i.e. when the fibre length is of the same order of magnitude as the flow domain. In particular, we showed the inadequacy of classical macroscopic models to address confinement conditions, which exhibit faster orientation rate than microscopic simulation based on the same physics.

In our previous work [13], we proposed a multi-scale description of rod orientation in confined conditions and simple shear flows. In this work, we extend the confined microscopic model within a second-gradient framework in order to address more realistic flows (i.e. parabolic velocity profiles encountered in Poiseuille or squeeze flows). We also consider the interaction of a rod with a single gap wall and predict "pole-vaulting" patterns as reported in experimental works [16]. Finally, we investigate the rheology of confined rod suspensions and discuss the problem of macroscopic descriptors in confined conditions

The paper is organized as follows: Section 2 is devoted to the derivation of a microscopic model for a confined fibre. This model is an extension of that introduced in [13] and is based on a dumbbell representation of a suspended fibre. In Section 3, the model is applied successively to Poiseuille and squeeze flows. Then, the issue of representing a confined suspension at the macroscopic scale is discussed in Section 4. Finally, the contribution of a confined rod to the rheology is considered in Section 5.

Remark 1. In this paper, we consider the following tensor products, assuming Einstein's summation convention:

- if $\mathbf{a}$ and $\mathbf{b}$ are first-order tensors, then the single contraction "$\cdot$" reads $(\mathbf{a}\cdot\mathbf{b}) = a_j\ b_j$;
- if $\mathbf{a}$ and $\mathbf{b}$ are first-order tensors, then the dyadic product "$\otimes$" reads $(\mathbf{a}\otimes\mathbf{b})_{jk} = a_j\ b_k$;
- if $\mathbf{a}$ and $\mathbf{b}$ are respectively second and first-order tensors, then the single contraction "$\cdot$" reads $(\mathbf{a}\cdot\mathbf{b})_j = a_{jm}\ b_m$;
- if $\mathbf{a}$ and $\mathbf{b}$ are second-order tensors, then the double contraction ":" reads $(\mathbf{a}:\mathbf{b}) = a_{jk}\ b_{kj}$;
- if $\mathbf{a}$ and $\mathbf{b}$ are respectively second and fourth-order tensors, then the double contraction ":" reads $(\mathbf{a}:\mathbf{b})_{jk} = a_{ml}\ b_{mljk}$.

2. Second-gradient modelling of confined fibres

We consider a Newtonian fluid of viscosity η and a non-Brownian, inertialess, high aspect ratio rod of length $2L$ immersed in it. The 3D-orientation of the rod is described by the unit vector $\mathbf{p}$ located at the rod centre of gravity G and aligned with its axis. We assume that the presence and orientation of the rod do not affect the flow velocity field defined by $\mathbf{v}$. The first and second gradient of the fluid velocity field are respectively denoted by $\nabla\mathbf{v}$ and $\mathbf{H}$.

The flow occurs in a narrow gap $\Omega\times[-H,H]$, with $[x\ y]\in\Omega\subseteq\mathbb{R}^2$ assumed large enough and $z\in[-H,H]$. Unless otherwise specified, we assume $H<L$ to ensure confinement conditions.

In the sequel, we consider the rigid dumbbell model to represent the rod [2,5], enriched with an extra bead located at its centre of gravity. The value of the hydrodynamic friction coefficient assigned to this extra bead is adjusted in order to ensure the hypothetical right rod motion as discussed below.

The use of the classical 2-bead representation would result in unmoving rods as soon as the end beads interact with the walls (since the fluid velocity vanishes at the domain boundaries in a Poiseuille flow). Such a situation was considered as unphysical and motivated the introduction of the third bead at the rod's centre of gravity. This extra bead ensures that the rod is experiencing the fluid flow at any time.

Each inertialess bead is subject to a hydrodynamic force (Stokes drag) due to the surrounding flow. An additional contact force appears on the external beads as soon as the rod touches the gap wall. Thus,

- The hydrodynamic force $\mathbf{F}^H$ acting on each bead depends on the difference of velocities between the fluid at the bead location and the bead itself. For the bead located at $\mathbf{p}L$, the former is given by $\mathbf{v}_0+\nabla\mathbf{v}\cdot\mathbf{p}L+\mathbf{H}:(\mathbf{p}\otimes\mathbf{p})L^2$ (with $\mathbf{v}_0$ the velocity of the fluid at the centre of gravity G) and the latter by $\mathbf{v}_G+\dot{\mathbf{p}}L$ (with $\mathbf{v}_G$ the velocity of the centre of gravity G). We consider here a second-gradient modelling framework and the components of $\mathbf{H}$ read $H_{ijk}=\frac{1}{2}\frac{\partial v_i}{\partial x_j\partial x_k}$. The hydrodynamic force acting on the bead located at $\mathbf{p}L$ reads
$$\mathbf{F}^H(\mathbf{p}L)=\xi\,(\mathbf{v}_0+\nabla\mathbf{v}\cdot\mathbf{p}L+\mathbf{H}:(\mathbf{p}\otimes\mathbf{p})L^2-\mathbf{v}_G-\dot{\mathbf{p}}L), \tag{5}$$
where ξ is a friction coefficient.
- The contact force is assumed to act perpendicularly to the wall:
$$\mathbf{F}^C(\mathbf{p}L)=\mu\mathbf{n}, \tag{6}$$
with $\mathbf{n}^T=[0\ 0\ 1]$ and $\mathbf{F}^C(\mathbf{p}L)=-\mathbf{F}^C(-\mathbf{p}L)$. The value of the intensity parameter μ is of course unknown and will be deduced from the underlying physics. In order to obtain it, we enforce that the contact force appears to prevent the rod from leaving the flow domain. In other words, the contact force $\mu\mathbf{n}$ must ensure that the resulting velocity is tangent to the upper surface, that is
$$(\mathbf{v}_G+\dot{\mathbf{p}}L)\cdot\mathbf{n}=0. \tag{7}$$
This equation is referred as the *impenetrability condition*.
- The friction force between the interacting bead and the wall, sacaling with the bead velocity, could also be added,
$$\mathbf{F}^F(\mathbf{p}L)=-\nu(\mathbf{v}_G+\dot{\mathbf{p}}L), \tag{8}$$
where ν is the friction coefficient at the wall. This frintion force is however not considered in the proposed model.

In the remainder of this section, we successively review the following scenarios: (i) the rod does not interact with the walls – unconfined motion (Fig. 1(a)); (ii) the rod interacts with one of the walls through one of its beads – wall effects (Fig. 1(b)); and (iii) both extremities of the rod are in contact with the gap walls – confined motion (Fig. 1(c)).

2.1. Unconfined motion

In the first scenario, the rod does not interact with the surrounding walls (Fig. 1(a)) and thus only hydrodynamic forces act on the beads.

The hydrodynamic forces on the three beads read
$$\mathbf{F}^H(\mathbf{p}L)=\xi\,(\mathbf{v}_0+\nabla\mathbf{v}\cdot\mathbf{p}L+\mathbf{H}:(\mathbf{p}\otimes\mathbf{p})L^2-\mathbf{v}_G-\dot{\mathbf{p}}L), \tag{9}$$

$$\mathbf{F}^H_G=\xi'(\mathbf{v}_0-\mathbf{v}_G), \tag{10}$$

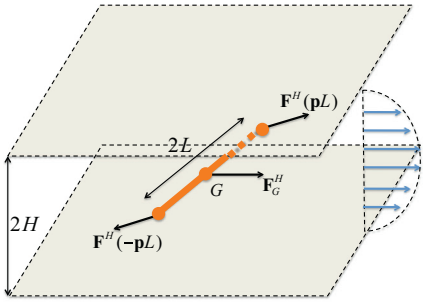

(a) Unconfined motion

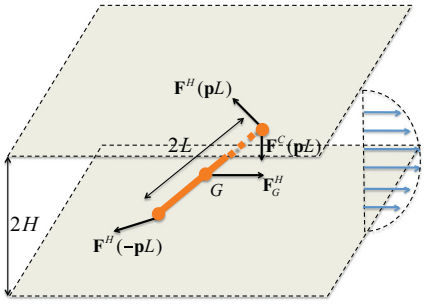

(b) Wall effects

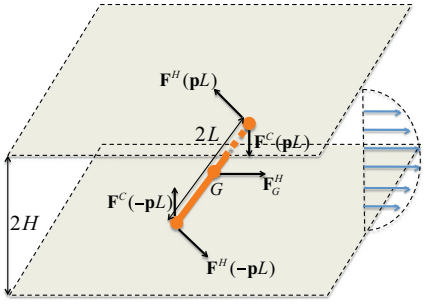

(c) Confined motion

Fig. 1. Forces acting on a suspended rod.

$$\mathbf{F}^H(-\mathbf{p}L) = \xi\,(\mathbf{v}_0 - \nabla\mathbf{v}\cdot\mathbf{p}L + \mathbf{H} : (\mathbf{p}\otimes\mathbf{p})L^2 - \mathbf{v}_G + \dot{\mathbf{p}}L), \tag{11}$$

where ξ and ξ' are friction coefficients.

On the one hand, balance of forces $\mathbf{F}^H(\mathbf{p}L) + \mathbf{F}^H(-\mathbf{p}L) + \mathbf{F}^H_G = \mathbf{0}$ yields

$$\mathbf{v}_G = \mathbf{v}_0 + \frac{2\xi}{2\xi+\xi'}\mathbf{H} : (\mathbf{p}\otimes\mathbf{p})L^2, \tag{12}$$

that is, the rod center of gravity has a relative velocity (drift) with respect to the fluid at this position

On the other hand, balance of torques provides the rod rotary velocity, which in this case is simply Jeffery's result $\dot{\mathbf{p}}^J$ for ellipsoids with infinite aspect ratio [11]:

$$\dot{\mathbf{p}} = \dot{\mathbf{p}}^J = \nabla\mathbf{v}\cdot\mathbf{p} - (\nabla\mathbf{v} : (\mathbf{p}\otimes\mathbf{p})\mathbf{p}). \tag{13}$$

The detailed derivation is given in [13] and is not modified neither by the second-gradient term, nor by the extra bead.

In order to obtain ξ', the friction coefficient assigned to the extra bead, we assume that the velocity of the rod centre of gravity is the same as if the hydrodynamic forces act *all along* the rod length [1]. At each position $\mathbf{p}s$, with $s \in [-L, L]$, the hydrodynamic force is now given by

$$\mathbf{F}^H(\mathbf{p}s) = \bar{\xi}\,(\mathbf{v}_0 + \nabla\mathbf{v}\cdot\mathbf{p}s + \mathbf{H} : (\mathbf{p}\otimes\mathbf{p})s^2 - \mathbf{v}_G - \dot{\mathbf{p}}s), \tag{14}$$

where the friction coefficient $\bar{\xi}$ is defined per unit of length.

With this approach, the balance of forces

$$\int_{-L}^{L}\mathbf{F}^H(\mathbf{p}s)\mathrm{d}s = \mathbf{0}, \tag{15}$$

implies that

$$2L\bar{\xi}\mathbf{v}_0 - 2L\bar{\xi}\mathbf{v}_G + \mathbf{H} : (\mathbf{p}\otimes\mathbf{p})\frac{2L^3\bar{\xi}}{3} = \mathbf{0}. \tag{16}$$

Comparing this equation with Eq. (12) leads to $\xi' = 4\xi$. We use this value in the remainder of this work.

2.2. Wall effects

In the second scenario, we consider (without any loss of generality) that the bead located at $\mathbf{p}L$ is in contact with the upper gap wall (Fig. 1(b)). The other beads remain in the fluid domain without interacting with the bottom wall.

The forces acting on the three beads read

$$\mathbf{F}^H(\mathbf{p}L) = \xi\,(\mathbf{v}_0 + \nabla\mathbf{v}\cdot\mathbf{p}L + \mathbf{H} : (\mathbf{p}\otimes\mathbf{p})L^2 - \mathbf{v}_G - \dot{\mathbf{p}}L), \tag{17}$$

$$\mathbf{F}^C(\mathbf{p}L) = \mu\mathbf{n}, \tag{18}$$

$$\mathbf{F}^H_G = \xi'(\mathbf{v}_0 - \mathbf{v}_G), \tag{19}$$

$$\mathbf{F}^H(-\mathbf{p}L) = \xi\,(\mathbf{v}_0 - \nabla\mathbf{v}\cdot\mathbf{p}L + \mathbf{H} : (\mathbf{p}\otimes\mathbf{p})L^2 - \mathbf{v}_G + \dot{\mathbf{p}}L), \tag{20}$$

where $\mathbf{F}^C$ is the contact force exerted by the wall on the bead and $\mathbf{n}^T = [0\ 0\ 1]$.

Again, balance of forces and torques lead respectively to an equation for the velocity of the centre of gravity

$$\mathbf{v}_G = \mathbf{v}_0 + \frac{2\xi}{2\xi+\xi'}\mathbf{H} : (\mathbf{p}\otimes\mathbf{p})L^2 + \frac{\mu}{2\xi+\xi'}\mathbf{n}, \tag{21}$$

and for the evolution of the rod orientation

$$\dot{\mathbf{p}} = \dot{\mathbf{p}}^J + \frac{\mu}{2\xi L}(\mathbf{n} - p_z\mathbf{p}). \tag{22}$$

The detailed derivation of the latter equation is given in Appendix A.

Imposing the impenetrability condition Eq. (7), we obtain the intensity μ of the contact force that prevents the rod from leaving the flow domain:

$$\mu = -\frac{2\xi L}{1-p_z^2}\left(\frac{1}{L}\mathbf{v}_G\cdot\mathbf{n} + [\dot{\mathbf{p}}^J]_z\right), \tag{23}$$

where $[\dot{\mathbf{p}}^J]_z = \dot{\mathbf{p}}^J\cdot\mathbf{n}$.

Using Eqs. (21)–(23), we can summarize the kinematics of a fibre having a single contact with a gap wall as follows:

$$\left(\mathbf{I} + \frac{2\xi}{2\xi+\xi'}\frac{\mathbf{n}\otimes\mathbf{n}}{(1-p_z^2)}\right)\mathbf{v}_G = \mathbf{v}_0 + \frac{2\xi}{2\xi+\xi'}\left(\mathbf{H} : (\mathbf{p}\otimes\mathbf{p})L^2 - \frac{L}{(1-p_z^2)}[\dot{\mathbf{p}}^J]_z\mathbf{n}\right), \tag{24}$$

and

$$\dot{\mathbf{p}} = \dot{\mathbf{p}}^J - \frac{1}{(1-p_z^2)}\left(\frac{1}{L}\mathbf{v}_G\cdot\mathbf{n} + [\dot{\mathbf{p}}^J]_z\right)(\mathbf{n} - p_z\mathbf{p}) = \dot{\mathbf{p}}^J + \dot{\mathbf{p}}^C. \tag{25}$$

The final result is simply Jeffery's kinematics $\dot{\mathbf{p}}^J$ plus a correction term $\dot{\mathbf{p}}^C$ that prevents the rod from leaving the flow domain. This expression for the rod rotary velocity is similar to the one we proposed in [13]. In other words, the orientation kinematics is the same whether one or both extremities of the rod interact with the gap walls and is not modified by the second-gradient description.

2.3. Confined motion

In the last scenario, both extremities of the rod are in contact with the gap walls (Fig. 1(c)). A contact force is now acting at each extremity of the rod.

The forces acting on the rod thus read

$$\mathbf{F}^H(\mathbf{p}L) = \xi(\mathbf{v}_0 + \nabla\mathbf{v}\cdot\mathbf{p}L + \mathbf{H} : (\mathbf{p}\otimes\mathbf{p})L^2 - \mathbf{v}_G - \dot{\mathbf{p}}L), \tag{26}$$

$$\mathbf{F}^C(\mathbf{p}L) = \mu\mathbf{n}, \tag{27}$$

$$\mathbf{F}^H_G = \xi'(\mathbf{v}_0 - \mathbf{v}_G), \tag{28}$$

$$\mathbf{F}^C(-\mathbf{p}L) = -\mu\mathbf{n}, \tag{29}$$

$$\mathbf{F}^H(-\mathbf{p}L) = \xi(\mathbf{v}_0 - \nabla\mathbf{v}\cdot\mathbf{p}L + \mathbf{H} : (\mathbf{p}\otimes\mathbf{p})L^2 - \mathbf{v}_G + \dot{\mathbf{p}}L). \tag{30}$$

This last scenario was similarly addressed in [13] and following the same rationale (impenetrability condition and balance of forces and torques), the velocity of the centre of gravity is given by

$$\mathbf{v}_G = \mathbf{v}_0 + \frac{2\xi}{2\xi+\xi'}\mathbf{H} : (\mathbf{p}\otimes\mathbf{p})L^2, \tag{31}$$

whereas the evolution of rod orientation follows

$$\dot{\mathbf{p}} = \dot{\mathbf{p}}^J + \frac{\mu}{\xi L}(\mathbf{n} - p_z\mathbf{p}), \tag{32}$$

with

$$\mu = -\frac{\xi L}{1-p_z^2}\left(\frac{1}{L}\mathbf{v}_G\cdot\mathbf{n} + [\dot{\mathbf{p}}^J]_z\right), \tag{33}$$

resulting in the same kinematics as in the case of wall effects (Eq. (25)).

3. Simulations in Poiseuille and squeeze flows

In this section, we present numerical simulations of the proposed model for confined suspensions in Poiseuille and squeeze flows. These flows, close to those encountered in real forming processes, exhibit a through-the-gap parabolic velocity profile that can be captured within the second-gradient framework.

3.1. Poiseuille flow

We first consider a parabolic Poiseuille flow, whose velocity field is expressed as $\mathbf{v}^T = [\beta(H^2 - z^2)\ 0\ 0]$, with $z \in [-H, H]$ and $\beta = 1$. The velocity vanishes at the walls.

We show here complete 3D-microscopic simulations, tracking the position, velocity and orientation of a handful of suspended rigid fibres. The initial orientation is set as $\theta_0 = \frac{2\pi}{5}$ (or the maximum possible value at that height in case this orientation is not possible due to the confining walls) in the $xz-$plane. In such case, the orientations remain in this plane.

Fig. 2 depicts the evolution of the position and orientation of short (left) and long (right) non-interacting fibres immersed in a Poiseuille flow. The fibres are represented by the blue lines, and the red curves show the trajectories of their centre of gravity.

In both cases, the fibres tend to align with the flow lines. During the orientation process, the upper fibres interact with the upper gap wall and are pulled away from it. In the case of short fibres, only the first (upper) rod interacts with the gap wall. As soon as the distance between the rod centre of gravity and the wall is L, the rod no longer moves away from the wall. This "pole-vaulting" pattern was observed experimentally by Stover and Cohen [16]. This feature is depicted in detail in Fig. 3. In the case of long fibres, the rods in the upper half of the domain first interact with the upper wall. The lower extremity of these rods gradually approaches the lower gap wall. As soon as both extremities are in contact with the domain boundaries, the rods no longer try to orient, and they slide on the frictionless walls. They are unable to align with the flow lines.

The initial orientation in the $xz-$plane proposed in this subsection (and the next one) is of course a special case, but it was chosen for the sake of clarity and visualization, in order to highlight the pole-vaulting patterns observed when a fibre interacts with a cavity wall. Initial orientations not aligned in the $xz-$plane also exhibit such behaviours but were difficult to rend on a static 2D plot and depend strongly on how fibres are initially oriented. Section 4 provides numerical results of the evolution of the orientation state starting from a general 3D orientation distribution.

3.2. Squeeze flow

We then consider a squeeze flow between two parallel disks. Initially, the disks are separated by a distance $2H_0$ and move with a constant velocity $\dot{h}$. We denote $h = h(t)$ the half-distance between the gap walls. Based on lubrication theory, the velocity field reads (in cylindrical coordinates) [5]:

$$\mathbf{v} = \begin{bmatrix} v_r \\ v_\theta \\ v_z \end{bmatrix} = \begin{bmatrix} \frac{3}{4}\frac{(-\dot{h})}{h} r\left[1 - \left(\frac{z}{h}\right)^2\right] \\ 0 \\ \frac{3}{2}\dot{h}\left[\left(\frac{z}{h}\right) - \frac{1}{3}\left(\frac{z}{h}\right)^3\right] \end{bmatrix}. \tag{34}$$

In this case, it is important to notice that the impenetrability condition Eq. (7) reads

$$(\mathbf{v}_G + \dot{\mathbf{p}}L)\cdot\mathbf{n} = \pm\dot{h}, \tag{35}$$

($+\dot{h}$ at the upper gap wall, $-\dot{h}$ at the lower gap wall), resulting in an additional term in the expression (23) of the contact force intensity μ.

Fig. 4 depicts the evolution of the position and orientation of short (left) and long (right) non-interacting fibres immersed in a squeeze flow. In such flow, intense interactions with the gap walls occur. The initial orientation is set as $\theta_0 = \frac{2\pi}{5}$ (or the maximum possible value at that height in case this orientation is not possible due to the confining walls) in the $xz-$plane. In such case, the orientations remain in this plane. Again, the fibres are represented by the blue lines, and the red curves show the trajectories of their centre of gravity.

4. Macroscopic descriptors for confined suspensions

At the macroscopic scale, the orientation of suspended particles is usually described by the second-order orientation tensor $\mathbf{a}$ [3]. In a continuous framework, this tensor is actually the second moment of the probability distribution function $\psi(\mathbf{p}, \mathbf{x}, t)$ that gives at each location and time, the fraction of particles aligned along direction $\mathbf{p}$:

$$\mathbf{a} = \int_{\mathcal{S}} (\mathbf{p}\otimes\mathbf{p})\psi(\mathbf{p})\mathrm{d}\mathbf{p}, \tag{36}$$

where $\mathcal{S}$ is the unit sphere on which $\mathbf{p}$ is defined. Using a discrete approach, this orientation tensor can be computed as an ensemble average over N suspended particles ($N \to \infty$):

$$\mathbf{a}^{\mathrm{discr}} = \frac{1}{N}\sum_{i=1}^{N} \mathbf{p}_i \otimes \mathbf{p}_i. \tag{37}$$

In our previous work [13], we showed that standard macroscopic models based on the second-order orientation tensor fail

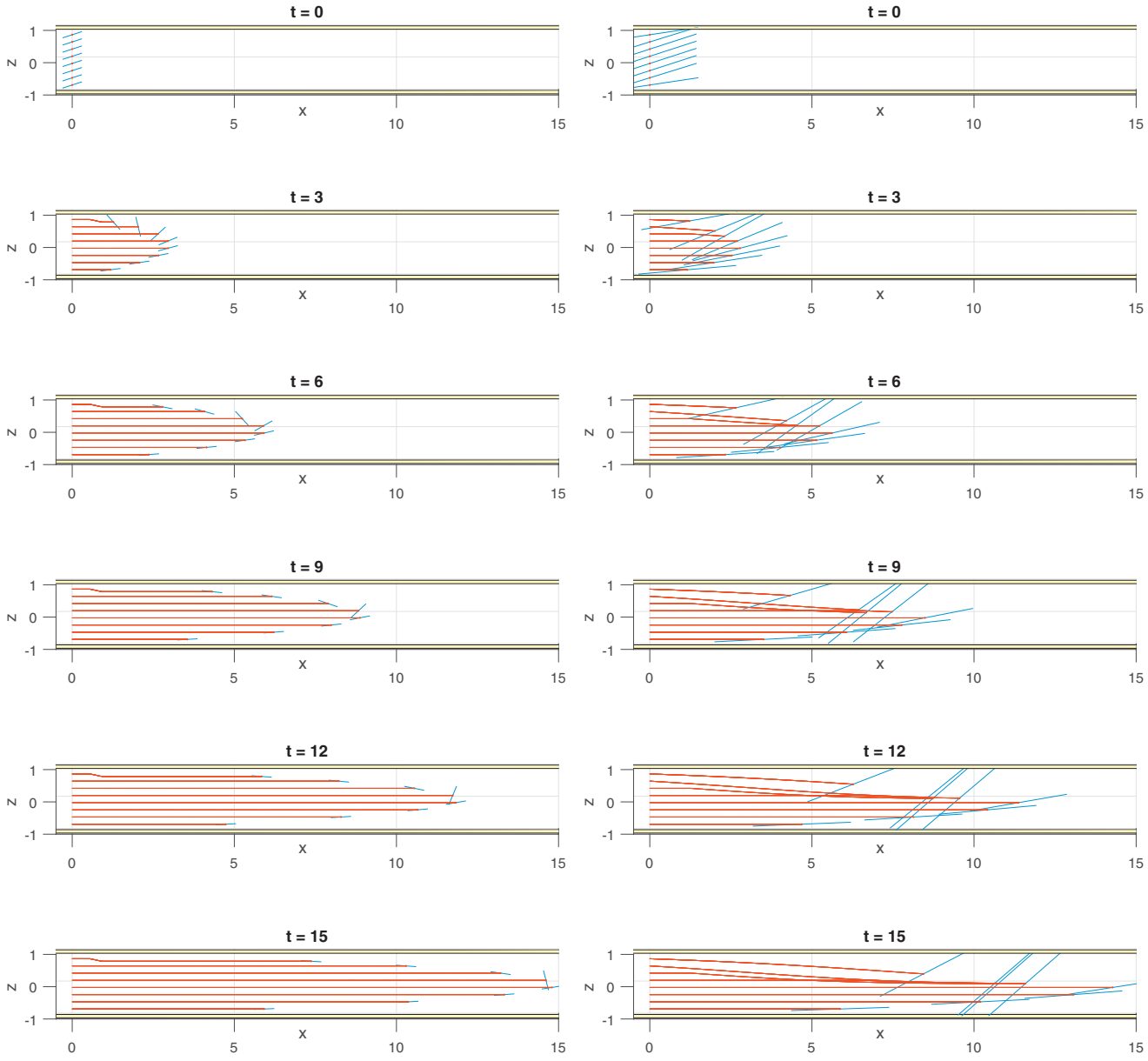

Fig. 2. Microscopic simulation of fibres immersed in a Poiseuille flow: (left) short fibres, $L = 0.3\ H$; (right) long fibres, $L = 1.5\ H$.

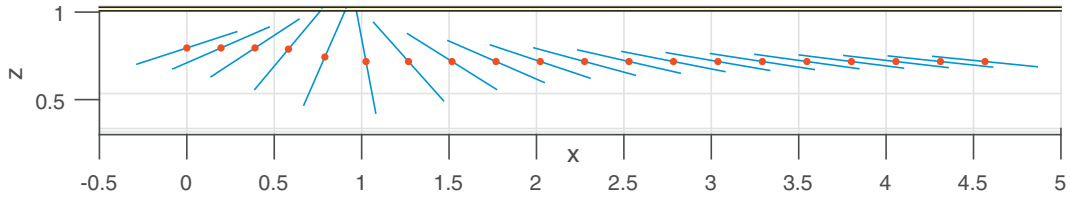

Fig. 3. Short fibre interacting with a gap wall - pole vaulting pattern. NB: It seems that the length of the fibre is not constant, but this is only an optical illusion.

to address confinement conditions. We would like to emphasize here that the second-order orientation tensor is not an adequate description of fibre orientation in confined suspensions.

In the case of confined suspensions, the length of the fibres is of the same order of magnitude than the narrow gap wherein the suspension flows. Thus, there is no separation of scales between what we usually refer to as the microscopic scale (the scale of the fibre) and the macroscopic scale (the scale of the process or the composite part). Under such conditions, the definition of standard macroscopic descriptors is ill-posed and a representative volume element (RVE) is hard to define. This issue appears when we consider a population of fibres and specify initial conditions for the fibre orientation. Defining an isotropic initial condition is ambiguous, because depending on the height of the fibre in the channel, the possible orientations are constrained. Our choice was thus to consider groups of fibres distributed along the channel height, in which fibres are oriented uniformly over the possible 3D orientations at that height (Fig. 5). Unless otherwise specified, we use

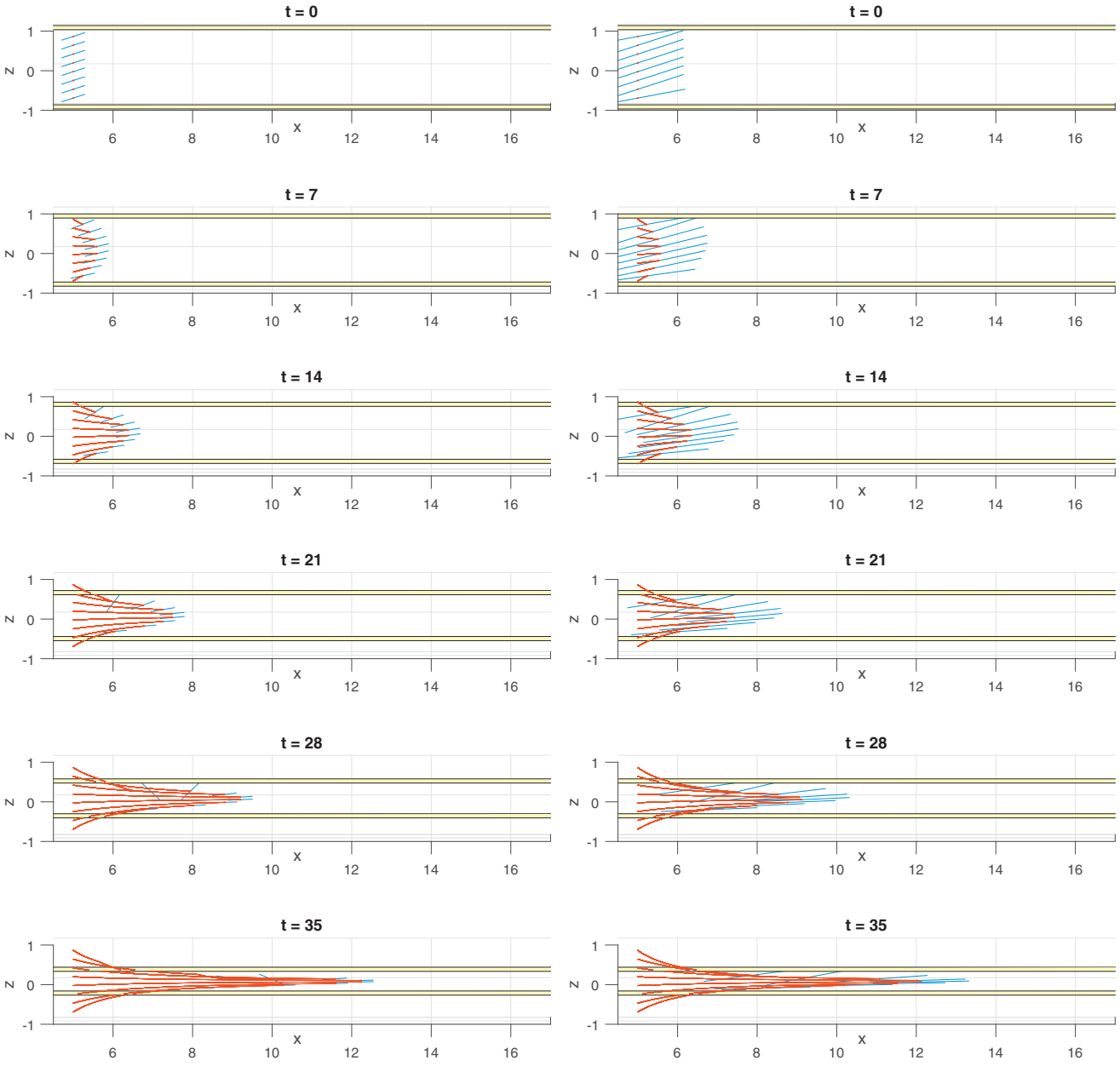

Fig. 4. Microscopic simulation of fibres immersed in a squeeze flow with $\frac{\dot{h}}{H_0} = -0.02\ s^{-1}$: (left) short fibres, $L = 0.3\ H_0$; (right) long fibres, $L = 1.2\ H_0$.

these initial orientations for simulations of populations of short and long fibres.

Figs. 6 and 8 show the evolution of the diagonal components of the second-orientation tensor (Eq. (37)) for a population of rods immersed in a Poiseuille and squeeze flow, respectively. As discussed in the previous paragraph, the initial condition consists in 10 groups of 50 fibres distributed along the channel height and oriented in the possible directions at that height (Fig. 5). This setting implies a significant disparity between the initial condition for short (left) and long (right) fibres.

In the case of a Poiseuille flow (Fig. 6), we find that all fibres tend to align in the direction of the flow. However, when considering long fibres (Fig. 6, right), the third component a_{zz} does not reach zero, meaning that the final state is not fully aligned with the flow lines. This behaviour was already evidenced in the previous section, however only a few fibres are unable to align.

Fig. 6 could suggest that the evolution of orientation for short and long fibres is radically different, meaning that size effects may play a role in the kinematic process. This interpretation is not correct. The difference actually arises from the change in the initial condition induced by confinement. As shown in Fig. 7, the evolution of a population of short fibres initially oriented as long fibres is similar to the kinematics of long fibres observed in Fig. 6 (right).

Considering now a squeeze flow, Fig. 8 could also suggest a significant difference between the kinematics of short and long fibres. A squeeze flow consists in compression and is not really elongational. Near the gap walls, the shearing nature of the flow is however dominating, and short fibres thus tend to align quickly in the flow, whereas in the middle of the channel, the motion is more like a rigid motion. This behaviour can be observed in Fig. 9 where only one group of short fibres is immersed in the middle of the flow. In this case, the first two diagonal components of the orien-

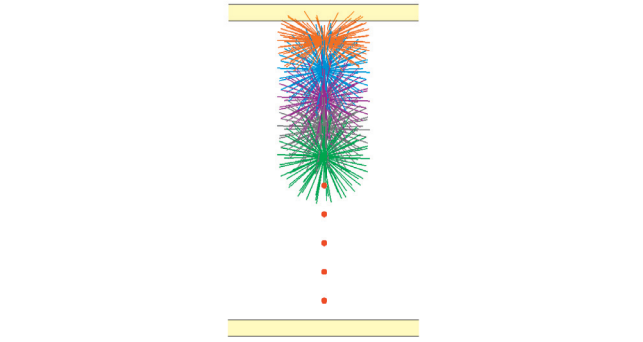

(a) Short fibres

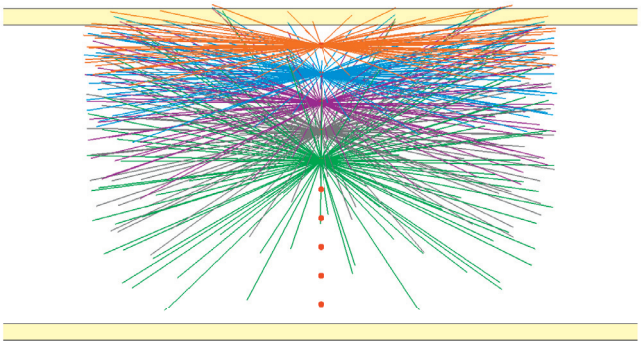

(b) Long fibres

Fig. 5. Initial orientation for a population of 10 groups of 50 fibres distributed along the channel height, in which fibres are oriented uniformly over the possible 3D orientations at that height. The lower half (not shown) is obtained by symmetry.

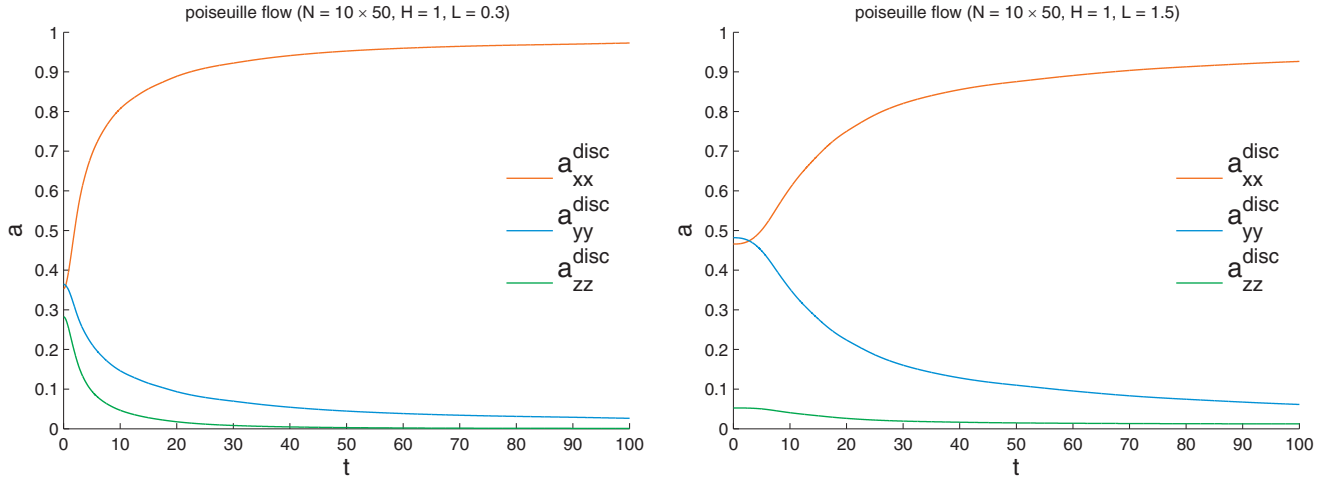

Fig. 6. Diagonal components of the orientation tensor for a population of $N = 500$ fibres immersed in a Poiseuille flow: (left) short fibres, $L = 0.3\ H$; (right) long fibres, $L = 1.5\ H$. Initial configurations are depicted in Fig. 5.

tation tensor do not evolve significantly, only the zz–component tends towards zero due to the compression.

5. Rheology of confined suspensions

In this section, we study the impact of confinement on the rheology of the dilute suspension. The contribution of a suspended particle to the stress is given by Kramers' formula [5]

$$\boldsymbol{\tau}^p = \mathbf{p}L \otimes \mathbf{F}(\mathbf{p}L) - \mathbf{p}L \otimes \mathbf{F}(-\mathbf{p}L), \tag{38}$$

where $\mathbf{F}(\pm\ \mathbf{p}L)$ is the total force acting on the bead located at position $\pm\ \mathbf{p}L$.

The extra-stress in the suspension due to the presence of the N suspended non-interacting particles is obtained by summing these

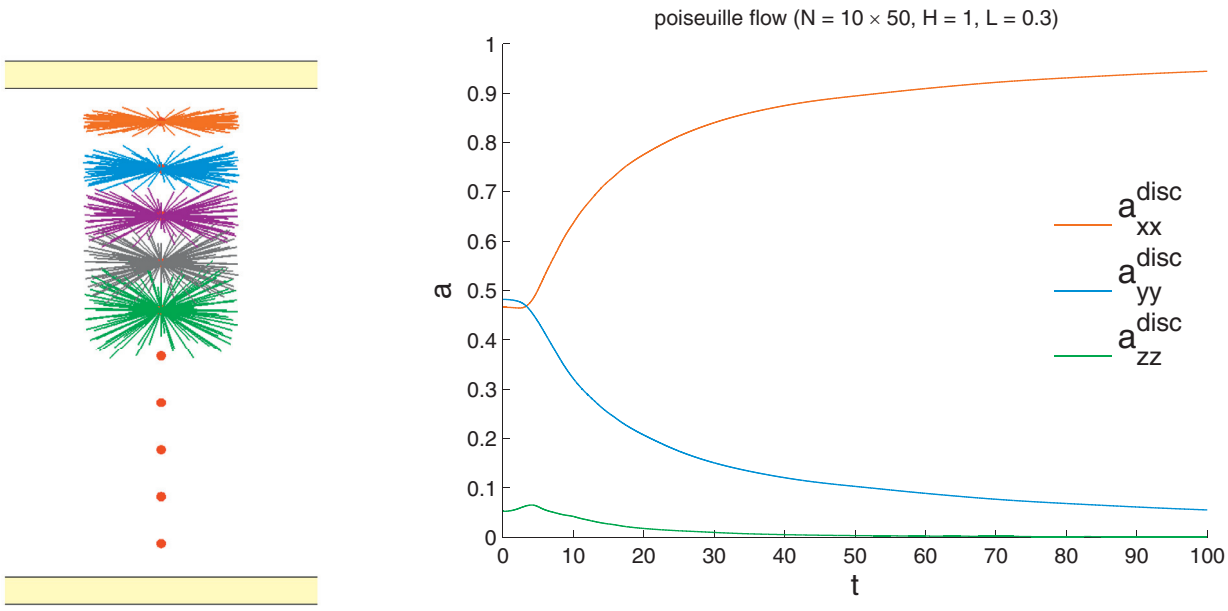

Fig. 7. (left) Initial condition (short fibres initially oriented as long fibres); (right) diagonal components of the orientation tensor for a population of $N = 500$ short fibres immersed in a Poiseuille flow ($L = 0.3\ H_0$).

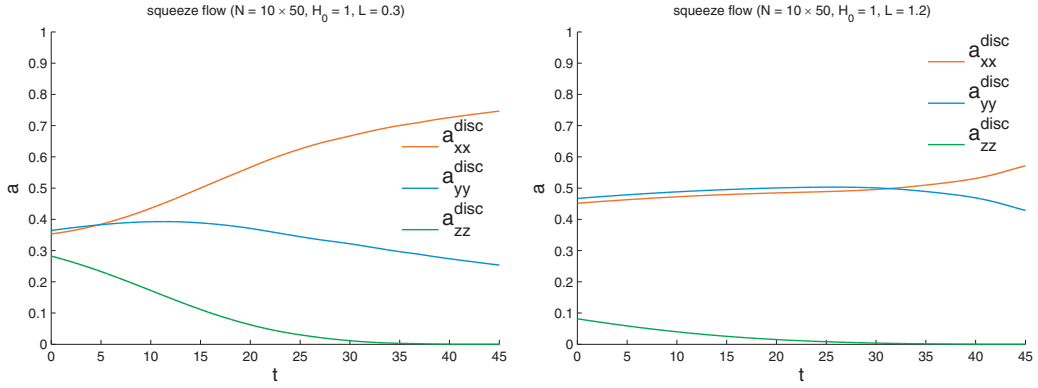

Fig. 8. Diagonal components of the orientation tensor for a population of $N = 500$ fibres immersed in a squeeze flow: (left) short fibres, $L = 0.3\ H_0$; (right) long fibres, $L = 1.2\ H_0$. Initial configurations are depicted in Fig. 5.

individual contributions:

$$\boldsymbol{\tau} = \sum_{i=1}^{N} \boldsymbol{\tau}^{p_i}. \tag{39}$$

5.1. Unconfined motion

In the case of unconfined motion, only hydrodynamic forces act on the rod and the well-known expression for the contribution of a single particle to the extra-stress in a fibre suspension is readily obtained:

$$\boldsymbol{\tau}^p = \boldsymbol{\tau}^{pJ} = \mathbf{p}L \otimes \mathbf{F}^H(\mathbf{p}L) - \mathbf{p}L \otimes \mathbf{F}^H(-\mathbf{p}L), \tag{40}$$

$$= 2\xi L^2(\nabla\mathbf{v} : (\mathbf{p}\otimes\mathbf{p}))\mathbf{p}\otimes\mathbf{p}, \tag{41}$$

$$= 2\xi L^2(\nabla\mathbf{v} : (\mathbf{p}\otimes\mathbf{p}\otimes\mathbf{p}\otimes\mathbf{p})), \tag{42}$$

where the $\mathbf{F}^H(\mathbf{p}L)$ is given by Eq. (17) and $\mathbf{p}$ follows Jeffery's kinematics Eq. (13).

5.2. Confined motion

When the particle interacts with the gap walls, additional contact forces act on the end beads. The particle contribution to the stress thus reads

$$\boldsymbol{\tau}^p = \mathbf{p}L \otimes (\mathbf{F}^H(\mathbf{p}L) + \mathbf{F}^C(\mathbf{p}L)) - \mathbf{p}L \otimes (\mathbf{F}^H(-\mathbf{p}L) + \mathbf{F}^C(-\mathbf{p}L)). \tag{43}$$

Inserting the confined kinematics (32) in the expression (17) of the hydrodynamic force, we can write

$$\mathbf{F}^H(\mathbf{p}L) = \xi(\mathbf{v}_0 + \mathbf{H} : (\mathbf{p}\otimes\mathbf{p})L^2 - \mathbf{v}_G) + \xi L(\nabla\mathbf{v} : (\mathbf{p}\otimes\mathbf{p}))\mathbf{p} - \mu(\mathbf{n} - p_z\mathbf{p}), \tag{44}$$

and

$$\mathbf{F}^H(\mathbf{p}L) + \mathbf{F}^C(\mathbf{p}L) = \xi(\mathbf{v}_0 + \mathbf{H} : (\mathbf{p}\otimes\mathbf{p})L^2 - \mathbf{v}_G) + \xi L(\nabla\mathbf{v} : (\mathbf{p}\otimes\mathbf{p}))\mathbf{p} + \mu p_z\mathbf{p}. \tag{45}$$

The particle contribution to the stress finally reads

$$\boldsymbol{\tau}^p = \underbrace{2\xi L^2(\nabla\mathbf{v} : (\mathbf{p}\otimes\mathbf{p}\otimes\mathbf{p}\otimes\mathbf{p}))}_{\boldsymbol{\tau}^{p,H}} + \underbrace{2\mu p_z(\mathbf{p}\otimes\mathbf{p})}_{\boldsymbol{\tau}^{p,C}} \tag{46}$$

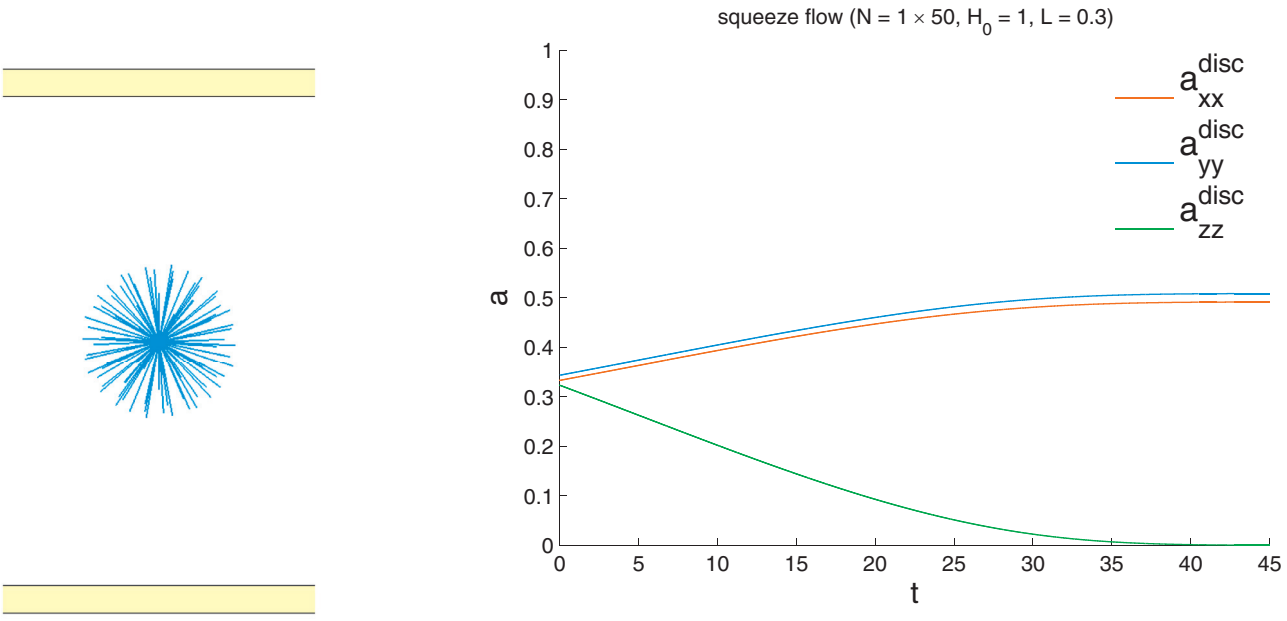

Fig. 9. (left) Initial condition (only one group of fibres at the centre of the channel); (right) diagonal components of the orientation tensor for a population of $N = 500$ short fibres immersed in a squeeze flow ($L = 0.3\ H_0$).

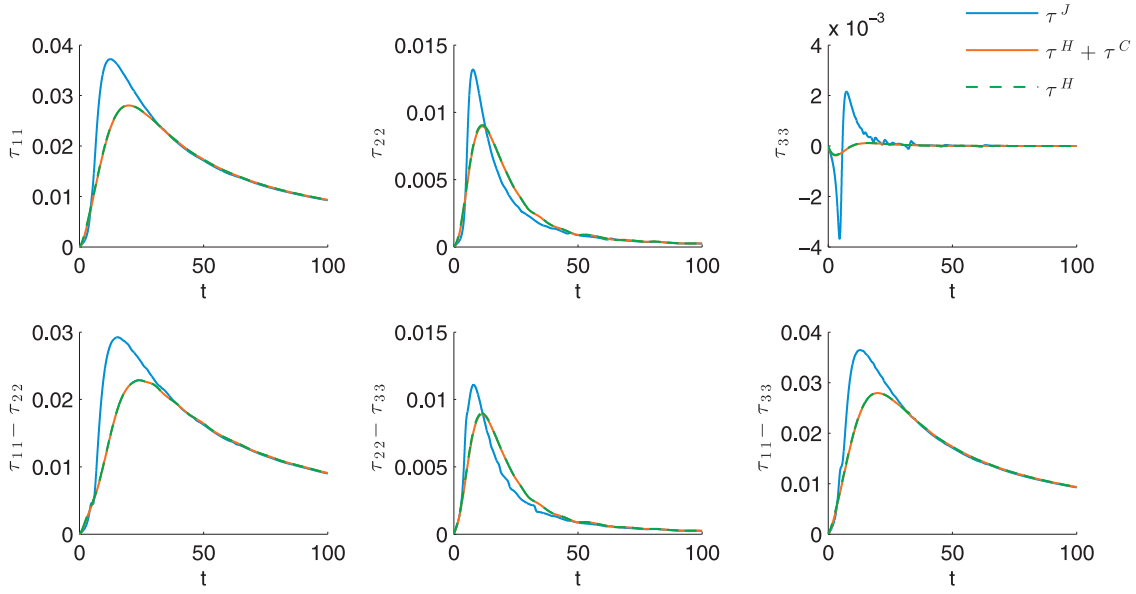

Fig. 10. Rheology of a confined suspension under a shear flow in a narrow gap ($H = 0.2L$). The orange curve shows $\boldsymbol{\tau} = \boldsymbol{\tau}^H + \boldsymbol{\tau}^C$, whereas the broken green curve shows only the classical hydrodynamic contribution $\boldsymbol{\tau}^H$. The blue curve depicts the rheology ($\boldsymbol{\tau}^J$) of hypothetical unconfined fibres following the standard Jeffery kinematics and starting from the same initial conditions. (For interpretation of the references to colour in this figure legend, the reader is referred to the web version of this article.)

with μ given by Eq. (33). It consists in a contribution $\boldsymbol{\tau}^{p,H}$ due to hydrodynamic forces and a contribution $\boldsymbol{\tau}^{p,C}$ arising from the contact forces induced by confinement.

5.3. Shear flow

We show here the impact of confinement on the rheology in the case of a simple shear flow, whose velocity field is expressed as $\mathbf{v}^T = [\dot{\gamma} z\ 0\ 0]$, with $z \in [-H, H]$ and $\dot{\gamma} = 1$.

Fig. 10 depicts the evolution of the normal stresses and normal stress differences for a population of $N = 2000$ rods of length L oriented uniformly along all possible orientations in a narrow gap of width $H = 0.2L$. The orange curve shows $\boldsymbol{\tau} = \boldsymbol{\tau}^H + \boldsymbol{\tau}^C$, whereas the broken green curve shows only the classical hydrodynamic contribution $\boldsymbol{\tau}^H$ (see Eq. (46)). We can observe that the contribution $\boldsymbol{\tau}^C$ can be neglected. Even when considering the contribution of a single particle to the stress, the contribution due to the contact force $\boldsymbol{\tau}^{p,C}$ is nearly zero. The blue curve depicts the rheology ($\boldsymbol{\tau}^J$) of hypothetical unconfined fibres following the standard Jeffery kinematics and starting from the same initial conditions. From Fig. 10, we thus conclude that confinement conditions have a significant impact on the rheology of confined suspensions. This impact does not arise from the contribution of the contact forces, but from the confined kinematics of the suspended fibres.

Fig. 11 depicts the evolution of non-diagonal component of the stress tensor τ_{13}, measuring the apparent viscosity $\eta = \frac{\tau_{13}}{\dot{\gamma}}$ of the suspension in this shear flow [12] with respect to time (or equiva-

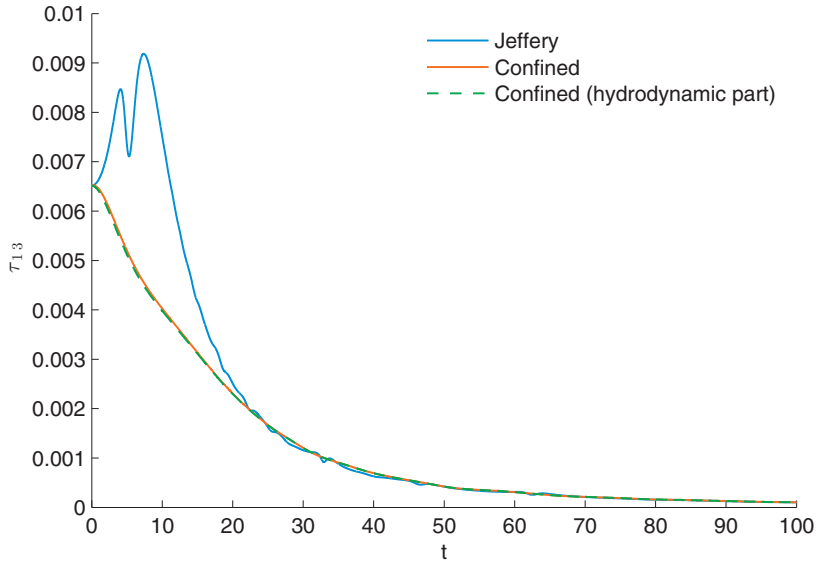

Fig. 11. Viscosity of a confined suspension under a shear flow in a narrow gap ($H = 0.2L$). The orange curve shows the evolution for the confined suspension, whereas the blue curve accounts for unconfined fibres starting from the same configurations. (For interpretation of the references to colour in this figure legend, the reader is referred to the web version of this article.)

lently, strain, since the strain rate $\dot{\gamma}$ is constant and equal to one). Once again, the orange curve shows the evolution for the confined suspension, whereas the blue curve accounts for unconfined fibres starting from the same configurations. We observe that, under confinement, the viscosity follows a monotonic evolution. The absence of overshoot is explained by the confinement configuration that prevents the fibres to directly tumble and align in the flow.

6. Conclusion and perspectives

In this paper, we have extended the modelling framework introduced in [13] to describe confined fibre suspensions. We have considered non-uniform strain rates at the scale of the fibre (second-gradient modelling) in order to address more complex flows. We showed that the orientation kinematics are the same whether one or both extremities of the rod interact with the gap walls. They consist in Jeffery's kinematics with an additional term to prevent the fibre from leaving the flow domain.

We applied our model to parabolic flows encountered in industrial applications (Poiseuille and squeeze flows), recovering behaviours observed in experimental works.

The use of macroscopic descriptors for confined suspensions remains a challenge. Standard representations (such as the second-order orientation tensor) appear to be inadequate under confinement conditions where separation of scale between the suspended particles and the scale of the flow is not established.

Finally, the impact of confinement on the rheology was investigated. We showed that the confined orientation of the particles significantly affects the rheology of the dilute suspension, but the impact of the wall contact force can be neglected.

Acknowledgements

A. Scheuer is a Research Fellow of the "Fonds de la Recherche Scientifique de Belgique" – F.R.S.-FNRS.

Appendix A. Detailed derivation of the confined kinematics

In the case of wall effects (only one contact with the gap walls), the forces acting on the beads are given by Eqs. (17)–(20). Balance of torques read

$$\mathbf{p}L \times (\mathbf{F}^H(\mathbf{p}L) + \mathbf{F}^C(\mathbf{p}L)) - \mathbf{p}L \times \mathbf{F}^H(-\mathbf{p}L) = \mathbf{0}. \tag{A.1}$$

Substituting the forces by their expression, we obtain

$$\mathbf{p}L \times \left(2\xi L(\nabla\mathbf{v}\cdot\mathbf{p} - \dot{\mathbf{p}}) + \mu\mathbf{n}\right) = \mathbf{0}, \tag{A.2}$$

or alternatively

$$2\xi L(\nabla\mathbf{v}\cdot\mathbf{p} - \dot{\mathbf{p}}) + \mu\mathbf{n} = \lambda\mathbf{p}, \tag{A.3}$$

with $\lambda \in \mathbb{R}$.

Pre-multiplying Eq. (A.3) by $\mathbf{p}$ and taking into account that fact that $\mathbf{p}$ is a unit vector, $\mathbf{p}\cdot\mathbf{p} = 1$ and thus $\mathbf{p}\cdot\dot{\mathbf{p}} = 0$, we obtain an expression for λ:

$$2\xi L(\nabla\mathbf{v} : (\mathbf{p}\otimes\mathbf{p})) + \mu p_z = \lambda, \tag{A.4}$$

with $p_z = \mathbf{p}\cdot\mathbf{n}$.

Finally, substituting Eq. (A.4) in Eq. (A.3) yields the orientation kinematics

$$2\xi L(\nabla\mathbf{v}\cdot\mathbf{p} - \dot{\mathbf{p}}) + \mu\mathbf{n} = 2\xi L(\nabla\mathbf{v} : (\mathbf{p}\otimes\mathbf{p}))\mathbf{p} + \mu p_z\mathbf{p}, \tag{A.5}$$

or

$$\dot{\mathbf{p}} = \underbrace{\nabla\mathbf{v}\cdot\mathbf{p} - \nabla\mathbf{v} : (\mathbf{p}\otimes\mathbf{p}))\mathbf{p}}_{\dot{\mathbf{p}}^J} + \frac{\mu}{2\xi L}(\mathbf{n} - p_z\mathbf{p}). \tag{A.6}$$

The derivation in the case of confinement (both extremities of the rod in contact with the gap walls) is obtained using the same rationale.

References

[1] E. Abisset-Chavanne, J. Ferec, G. Ausias, E. Cueto, F. Chinesta, R. Keunings, A second-gradient theory of dilute suspensions of flexible rods in a Newtonian fluid, Arch. Comput. Methods Eng. 22 (2015) 511–527.
[2] E. Abisset-Chavanne, F. Chinesta, J. Ferec, G. Ausias, R. Keunings, On the multiscale description of dilute suspensions of non-Brownian rigid clusters composed of rods, J. Non-Newtonian Fluid Mech. 222 (2015) 34–44.
[3] S. Advani, C. Tucker, The use of tensors to describe and predict fiber orientation in short fiber composites, J. Rheol. 31 (1987) 751–784.
[4] G.K. Batchelor, The stress system in a suspension of force-free particles, J. Fluid Mech. 41 (1970) 545–570.
[5] R.B. Bird, C.F. Curtiss, R.C. Armstrong, O. Hassager, Dynamic of Polymeric Liquid, Kinetic Theory, 2, John Wiley and Sons, 1987.

[6] J. Ferec, G. Ausias, M.C. Heuzey, P. Carreau, Modeling fiber interactions in semi-concentrated fiber suspensions, J. Rheol. 53/1 (2009) 49–72.
[7] F. Folgar, C. Tucker, Orientation behavior of fibers in concentrated suspensions, J. Reinf. Plast. Comp. 3 (1984) 98–119.
[8] J. Hinch, G. Leal, The effect of Brownian motion on the rheological properties of a suspension of non-spherical particles, J. Fluid Mech. 52 (1972) 683–712.
[9] J. Hinch, G. Leal, Constitutive equations in suspension mechanics, Part I, J. Fluid Mech. 71 (1975) 481–495.
[10] J. Hinch, G. Leal, Constitutive equations in suspension mechanics, Part II, J. Fluid Mech. 76 (1976) 187–208.
[11] G.B. Jeffery, The motion of ellipsoidal particles immersed in a viscous fluid, Proc. R. Soc. London A102 (1922) 161–179.
[12] S. Mueller, E.W. Llewellin, H.M. Mader, The rheology of suspensions of solid particles, Proc. R. Soc. London A466 (2010) 1201–1228.
[13] M. Perez, A. Scheuer, E. Abisset-Chavanne, F. Chinesta, R. Keunings, A multi-scale description of orientation in simple shear flows of confined rod suspensions, J. Non-Newtonian Fluid Mech. 233 (2016) 61–74.
[14] C. Petrie, The rheology of fibre suspensions, J. Non-Newtonian Fluid Mech. 87 (1999) 369–402.
[15] J. Phelps, C. Tucker, An anisotropic rotary diffusion model for fiber orientation in short and long fiber thermoplastics, J. Non-Newtonian Fluid Mech. 156/3 (2009) 165–176.
[16] C.A. Stover, C. Cohen, The motion of rodlike particles in the pressure-driven flow between two flat plates, Rheol. Acta. 29 (1990) 192–203.
[17] J. Wang, C.A. Silva, J.C. Viana, F.W.J. van Hattum, A.M. Cunha, C. Tucker, Prediction of fiber orientation in a rotating compressing and expanding mold, Polym. Eng. Sci. (2008) 1405–1413.
[18] J. Wang, J. O'Gara, C. Tucker, An objective model for slow orientation kinetics in concentrated fiber suspensions: theory and rheological evidence, J. Rheol. 52/5 (2008) 1179–1200.